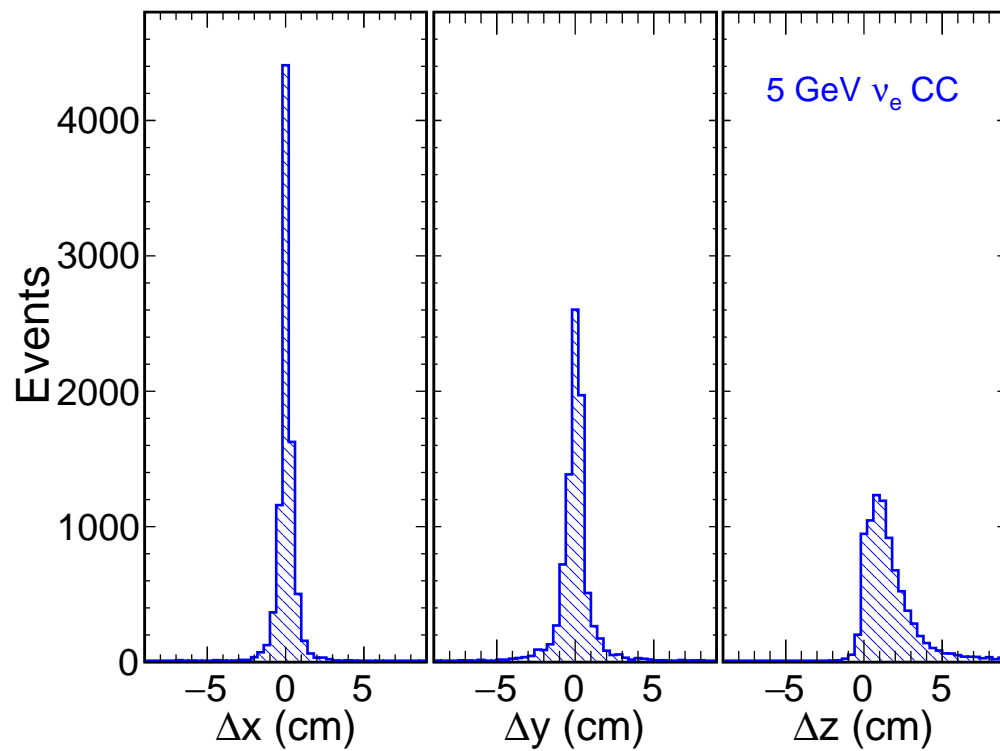


Annex 4C: Simulation and Reconstruction

Long-Baseline Neutrino Facility (LBNF) and Deep Underground Neutrino Experiment (DUNE)



August 14, 2015

Contents

2	1 Simulation	1
3	1.1 Near Detector Simulation	1
4	1.2 Far Detector Simulation	1
5	1.2.1 Single-Phase Detector Modeling	3
6	1.2.2 Dual-Phase Detector Modeling	4
7	2 Reconstruction	6
8	2.1 Near Detector Reconstruction	6
9	2.2 Far Detector Reconstruction	7
10	2.2.1 Signal Processing and Filtering	7
11	Single-Phase Signal Processing and Filtering	7
12	Dual-Phase Signal Processing and Filtering	9
13	2.2.2 TPC Hit Finding	9
14	Single-Phase Hit Finding	10
15	Dual-Phase Hit Finding	10
16	Single-Phase Disambiguation	10
17	2.2.3 Optical Detector Signal Reconstruction	11
18	2.2.4 TPC Hit Clustering	13
19	2.2.5 Track Fitting	15
20	2.2.6 Shower Measurement	18
21	2.2.7 Calorimetry	20
22	2.2.8 Particle Identification	20
23	2.2.9 Neutrino Event Reconstruction and Classification	20
24	2.2.10 Calibration	23

List of Figures

2	1.1	Far detector simulation block diagram	2
3	2.1	Far detector reconstruction block diagram	8
4	2.2	Disambiguation performance	12
5	2.3	PANDORA event displays	16
6	2.4	PANDORA reconstruction efficiency	17
7	2.5	PANDORA purity and completeness	17
8	2.6	PANDORA vertex resolution	18
9	2.7	Vertex reconstruction using local principal curves	19
10	2.8	Performance of dE/dx -based $e - \gamma$ separation vs S/N	21
11	2.9	Performance of dE/dx -based $e - \gamma$ separation vs Energy	22
12	2.10	LAGNUA-LBNO event classification	23
13	2.11	LAGNUA-LBNO electron neutrino energy measurement	24
14	2.12	LAGNUA-LBNO muon neutrino energy measurement	24

¹ List of Tables

1 **Todo list**

2	To be supplied, even if short	1
3	To be supplied, even if it is brief	6
4	Not sure whether or not to mention LArSoft and Qscan explicitly here	7
5	Hit-finder performance plot?	10
6	In the single-phase reconstruction, the availability of three views provides strong constraints on	
7	3D ambiguities	14
8	CLUSTERING/PANDORA FOR LBNO (TWO VIEWS), taken from LGUNA-LBNO deliverables	
9	document	14
10	Overflow from CDR:	15
11	Can we say something about current status or performance?	18
12	Talk about e-gamma separation here	20
13	Talk about event classification here:	20

Chapter 1

Simulation

Simulated data samples provide the basis for detailed studies of detector performance, inform detector design choices, and enable the development of automated event reconstruction. Detailed Monte Carlo predictions of expected data distributions will also be needed in order to extract physics results from the DUNE experiment. Several important sources of systematic uncertainty come from detector modeling, and varying the assumptions incorporated in the simulations provides the mechanism by which these systematic uncertainties can be estimated. Simulations are needed in order to extrapolate from auxiliary data samples, such as testbeam measurements or *in situ* measurements using events not passing signal event selection requirements, to the signal selection samples. The following sections describe the simulation of the Near and Far Detectors.

1.1 Near Detector Simulation

1.1.1 Parametrized simulation

The DUNE Near Neutrino Detector (NND) parametrized simulation and reconstruction (ND FastMC) has been developed to explore the sensitivities of near detector physics. The Near Detector FastMC is an extension to the Far Detector FastMC [?], Appendix A.3. The ND FastMC combines the Geant4 simulation of the beamline, the GENIE [10] neutrino interaction model, and a parameterized detector response that is used to simulate the measured (reconstructed) energy and momentum of each final-state particle. The detector response is based on the NOMAD detector simulation and reconstruction as the reference NND design is built upon the NOMAD detector, but with much higher resolution.

As the NND is vastly different from FD, the following features have been added into the ND FastMC. The first feature is the magnetic field. The 4th order Runge-Kutta method which is used by Geant4 simulation has been incorporated in the ND FastMC. Fig. ?? shows the trajectories of muon passing through the detector. From top left to bottom right, the plots are μ^+ with 1 GeV kinetic energy, μ^- with 1 GeV kinetic energy, μ^+ with 0.2 GeV kinetic energy, μ^- with 0.2 GeV

kinetic energy, respectively. The second feature is to model the energy deposited in the detector as the particle travels through, dE/dx . A standalone Geant4 application was developed with a simplified detector description of Straw Tube Tracker. Using the Geant4 particle gun, e^\pm , π^\pm , μ^\pm , K^\pm , proton were shot and propagated through this simplified detector and the information of dE/dx as a function of their kinetic energy were recorded as a 2 dimensional histogram as shown in Fig. ???. In the ND FastMC, a final-state particle produced by a neutrino-nucleon interaction deposits energy when it is traveling through the detector. The amount of energy deposited, dE/dx , would be calculated by calling a ROOT method given the particle's kinetic energy, T_K . The stepping continues until either the particle loses all its energy and stops or exits the detector. Special care is paid to the π^0 reconstruction as it may be a potential background to the neutrino electron scattering when the photons from π^0 decay undergo asymmetric conversion producing a single electron track.

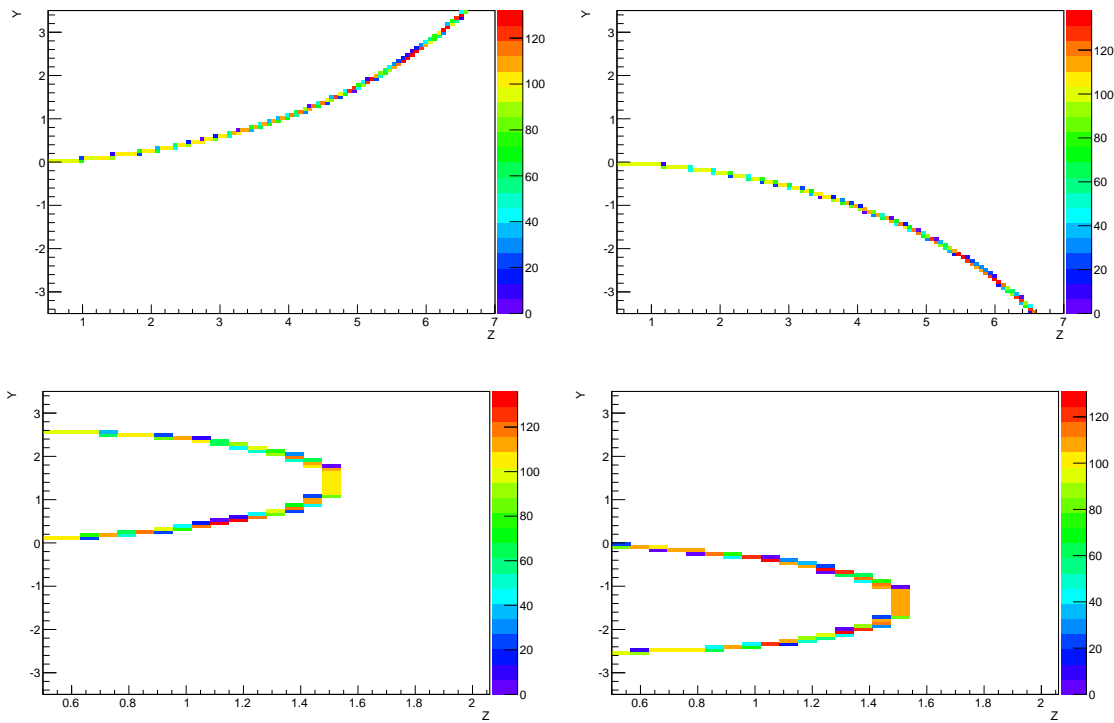


Figure 1.1: Muons trajectories in the near detector's magnetic field in $y - z$ view. The magnetic field is 0.4 pointing perpendicularly into the paper. Top left: μ^+ with 1 GeV kinetic energy; top right: μ^- with 1 GeV kinetic energy; bottom left: μ^+ with 0.2 GeV kinetic energy; bottom right: μ^- with 0.2 GeV kinetic energy.

fig:ndfa

1.1.2 Geant4-based simulation

The full Geant4-based detector simulation and reconstruction algorithms are still under development. HiSoft (High-resolution FGT Software) is similar to the FD simulation and reconstruction framework, LArSoft. It is based on the Art-framework for event management and NuTools for interfacing with Geant4. Git repositories serve as the version control, and multi-repository build tool

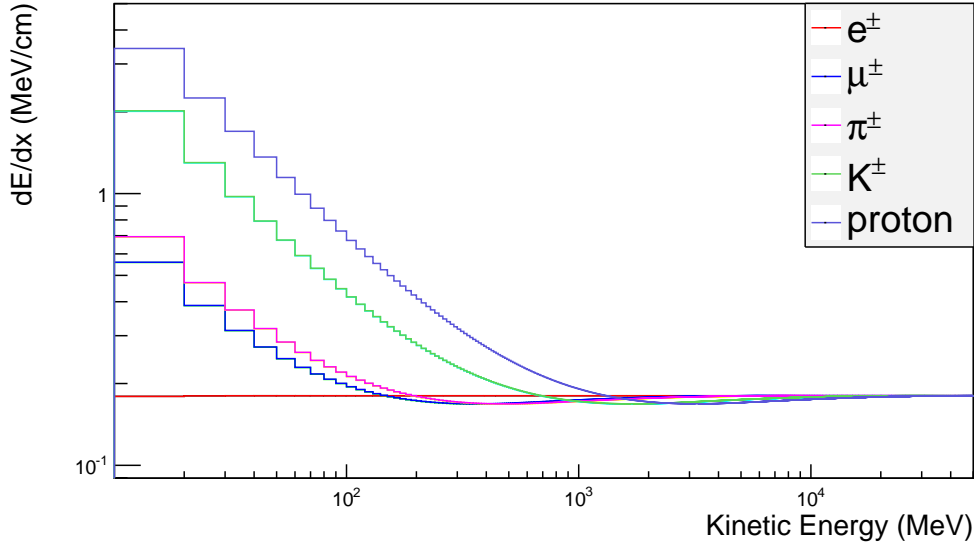


Figure 1.2: dE/dx vs kinetic energy distribution for individual particles produced by a standalone Geant4 application

fig:ndfa

Table 1.1: Summary of the parameters used in the ND FastMC.

Internal Magnetic Volume	$4.0 \times 4.0 \times 8.1$ m
Tracker volume (STT)	$3.5 \times 3.5 \times 7.04$ m, density = 0.1 g/cm ³
Fiducial volume	$ x, y < 150$ cm, $25 < z < 550$ cm
Radiation length	$X_0 \simeq 600$ cm
hadronic interaction length	1,200 cm
Charged particle momentum resolution	$\sigma_p/p = \frac{0.05}{\sqrt{L}} + 0.008p/\sqrt{L^5}$, L : track length
Angular resolution	$\theta_0 = \frac{13.6 \text{ MeV}}{\beta_{cp}} z \sqrt{x/X_0} [1 + 0.038 \ln(x/X_0)]$
EM shower energy resolution	$\sigma_E/E = 1\% + 0.06/\sqrt{E}$
Hadronic shower energy resolution	$\sigma_E/E = 1\% + 0.50/\sqrt{E}$

b:ndfastmc_par

(MRB) has been using to configure and compile the software, though there is only one repository thus far.

The geometry described by Geometry Description Markup Language (GDML) is shown in Fig. ???. The GDML file is generated by a python script which has the flexibility of varying the parameters in order for the detector optimization study. A test module in the Geometry package has been developed to ensure proper spacings/sortings of the straw tubes. The geometry interface service fulfilling all needs of Geant4 simulation exists. A Geant4 user action saves particle trajectory information and the simulated space charge (FIG. ??) saved per straw tube in a way to make channel digitization most effective and allow for backtracking to simulated information during assessment of reconstruction. Over the next years, increasing effort will be directed at the detector optimization using Geant4.

fig:ndgeo

fig:ndsim_mu

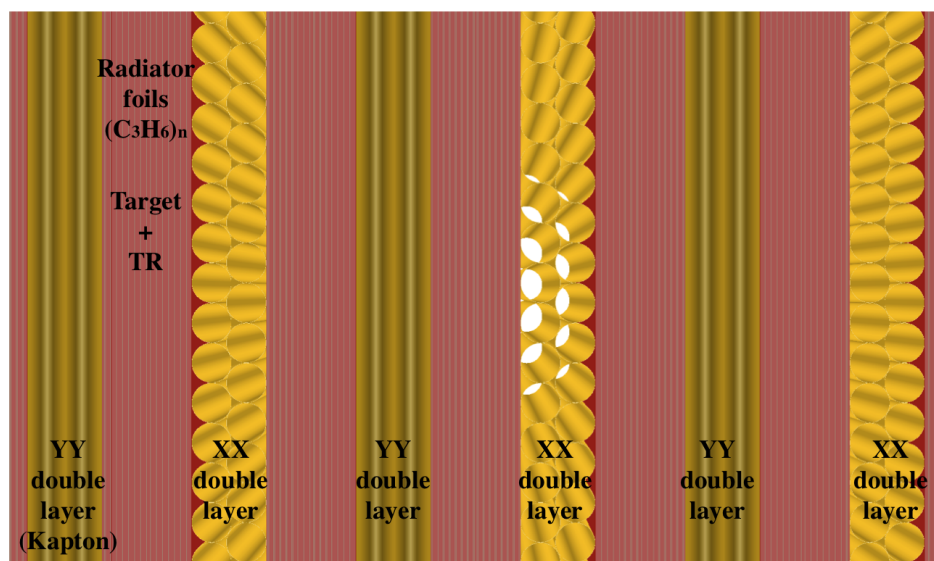


Figure 1.3: Near Detector STT geometry described in GDML

fig:ndge

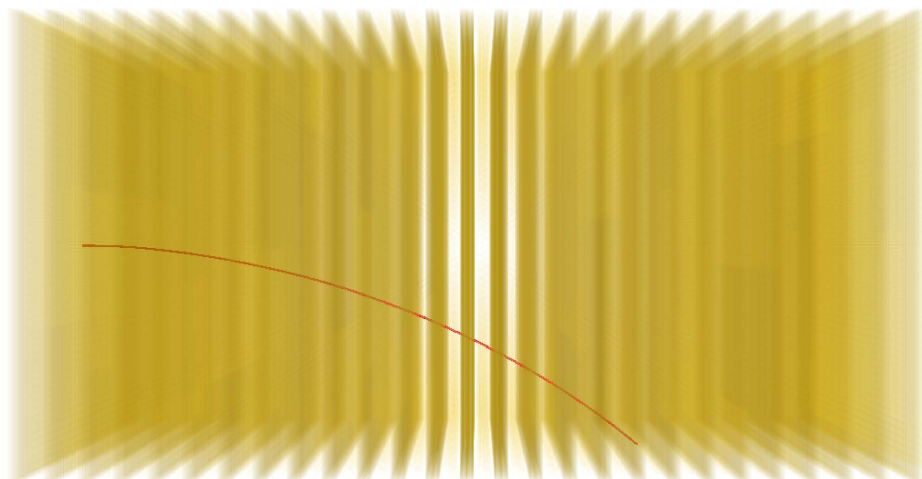
Figure 1.4: The trajectory of a 1 GeV μ^- produced by HiSoft simulation

fig:ndsi

1.2 Far Detector Simulation

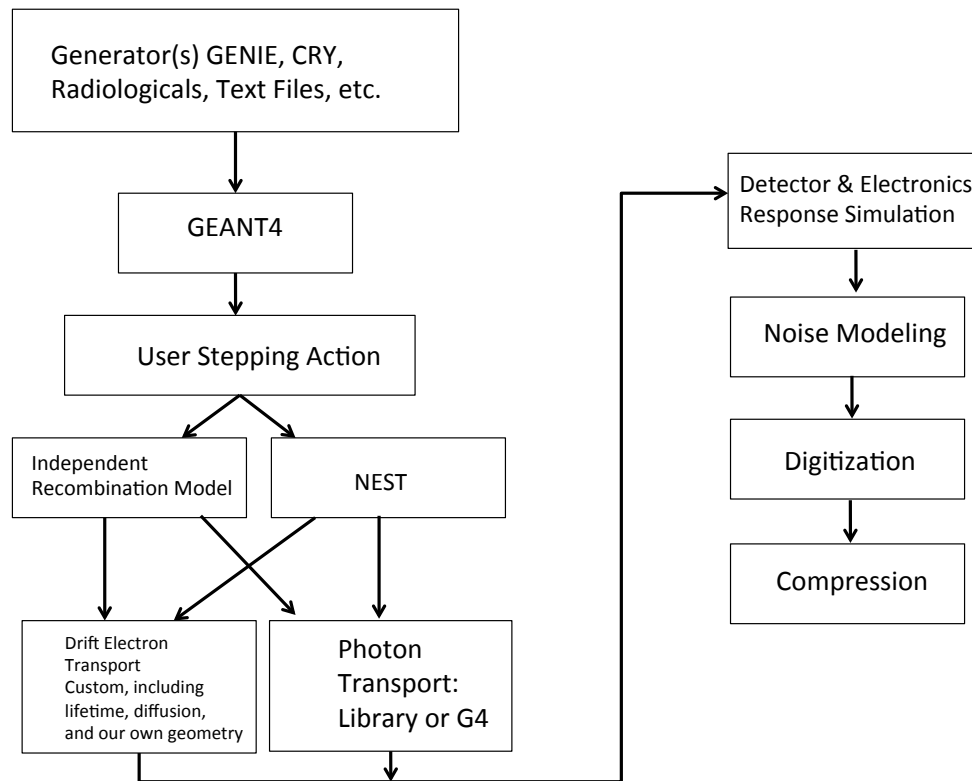


Figure 1.5: Block diagram showing the components of the far detector simulation chain

fig:fdsi

Monte-Carlo simulations of liquid-argon TPC detectors have reached a level of maturity in the last decade. Detailed GEANT4-based [1, 2] simulation programs have been developed for both the single-phase and dual-phase Far Detector designs, incorporating both the Liquid Argon TPC modules and the photon detection systems.

The single-phase detector simulation is implemented in LArSoft, which provides a common simulation framework for Liquid Argon TPC experiments. Confidence in the simulation capabilities is improved by the comparison of data from ArgoNeuT [3, 4, 5, ?] with LArSoft simulations. Future data from LArIAT [3, 6], MicroBooNE [7, 8, 9], and the 35-ton prototype will allow further tuning of the LArSoft simulation as experience is gained. The dual-phase detector simulation is based on the Qscan package, which has been developed over the past decade, and is currently being used to perform technical design and physics studies for the WA105 program.

Events are generated using the GENIE [10] neutrino-nucleus simulation program, the CRY [11, 12, 13] cosmic-ray generator, a custom radiological decay simulator, a particle gun, or one of several text-file-based particle input sources. The interactions of particles with the liquid argon

and other detector materials is simulated with GEANT4. A flexible geometry description interface is provided using GDML [14] files that can be altered as the detector design evolves. GEANT4 is used to simulate energy deposits in each step of each particle, and custom routines have been written to translate these into numbers of ionization electrons and scintillation photons produced in the liquid argon. Two ionization models are available: a simple parameterization that scales electrons and photons with energy using a modified Birks recombination model [15, 16], and NEST [17, 18], a more detailed simulation that incorporates the expected statistical anticorrelation between scintillation photons and drifting electrons, and which has been tuned to match available noble liquid detector data.

1.2.1 Single-Phase Detector Modeling

The drifting electrons are propagated using dedicated code that numerically integrates over the diffusion probabilities, includes the effect of finite electron lifetime, and selects the wire on which to deposit the charge. A parameterization of the distortions expected from average values of space charge accumulations is also modeled, though the main impact of this will be seen in the 35-ton prototype and liquid argon TPC detectors on the surface, such as MicroBooNE and LArIAT. Information is saved in memory and written to the simulation output file of where each parcel of charge on each wire originated, and what the GEANT particle ID was that generated that charge.

Propagating photons are simulated using a lookup table that is filled with the probabilities for detecting a photon in a specific detector channel when it is emitted at a point in space, where the detector channels and a binning of the point in space serve as indices to the lookup table. This table is filled using fully simulated photons propagated with GEANT4, including the effects of Rayleigh scattering, reflection, and absorption on the detector surfaces. Broadening of photons arrival time (due to multiple Rayleigh scatterings) is also parametrised and such information can be retrieved at simulation time to properly reproduce the features of time signal. The detection probabilities for photons striking the sensitive materials of the photon detectors is separately parameterized.

Signals on the TPC wires and photon detectors are then convoluted with the expected response functions, which include the induced charge vs. time functions and the electronics response functions, parameterized noise is added, and the result is saved as simulated ADC values vs. time, where digitization is simulated at 2 MHz for the TPC wires and 150 MHz for the photon detectors, including the effects of saturation of the ADC's. The bipolar induction-plane signals and the unipolar collection-plane signals are simulated separately. Induced charge on neighboring collection wires has a bipolar component to it and is added to the unipolar direct collection signal. Events are defined to be at least one drift window long, though much longer events are needed in order to sample interactions that happen near the edges in either space or time. Zero suppression and Huffman coding of the data are applied as options. The data are stored in ROOT files using the compression algorithms available in ROOT.

1.2.2 Dual-Phase Detector Modeling

In a dual-phase liquid argon detector, the TPC signal amplification is based on the charge multiplication in argon vapor due to the Townsend effect, i.e. drifting electrons gain enough energy in a strong electric field to further ionize argon atoms. The readout system consists of an extraction grid, a Large Electron Multiplier (LEM) and two views anode. For such technology, additional processes contribute to the accumulation of space charge, hence to the actual electric field in the liquid active volume. In particular, in the charge multiplication process, there is a formation of positive argon ions, that drift back towards the active volume. A significant part is collected on the bottom electrode of the LEM and on the extraction grid. The ions that enter into the liquid phase contribute to the positive charge distribution. The local value of the electric charge density and the three components of the electric field are computed using a three-dimensional time-dependent finite element analysis calculation of the equilibrium configuration of a physical system where the differential equations describing each charge production (e.g.: ionisation, amplification) and absorption (e.g.: recombination, attachment) process are solved simultaneously. A lookup table is then used in Qscan at simulation/reconstruction level in order to associate to a given point in the active detector volume the channels where the charge will be deposited on the readout plane as well as the drift time.

Light readout system in the dual-phase liquid argon TPC consists of an array of cryogenic photomultipliers (PMT). The PMT components, both the reflecting surfaces and the sensitive elements, are simulated in GEANT4. Moreover, the PMT detector surface is coated with a layer of wavelength shifting (WLS) material which converts a scintillation photon (optical UV photon) into a visible photon. The WLS behaviour is fully simulated in terms of absorption probability as well as emission spectrum. The dependence of the collection efficiency on the photon incident angle is also taken into account on the base of the existing measurements.

A lookup table is used to calculate the probability for a photon emitted in a given volume element to be detected by a specific PMT. Broadening of photons arrival time (due to multiple Rayleigh scatterings) is also parametrised and such information can be retrieved at simulation time to properly reproduce the features of time signal.

For each detected photon a voltage signal is simulated following the results of dedicated measurements showing that a typical PMT response can be approximated with a log-normal distribution. Similarly, the charge integral of the produced signal is sampled from a distribution extracted from data obtained during calibration measurements performed on the specific PMT model.

For the complete treatment of the light production in a dual-phase TPC the secondary scintillation light must be taken into account as well. Secondary scintillation process refers to light produced in the gas phase of the detector when electrons, extracted from the liquid, are accelerated. Scintillation in argon gas is simulated through a parameterization to the existing measurements of secondary scintillation light yields.

Signal on the charge readout plane is simulated in Qscan through a waveform generation stage where the MC truth information is converted into a readout signal. The finally recorded signal is a convolution of the induced current and the response of the preamplifier. In the case of a

LEM readout, a collection plane that records unipolar signals, due to the fast electron drift in gas and the short induction gap between LEM and 2D anode, the induced current approaches a δ -function and the signal is directly given by the fast response of the preamplifier. The recorded voltage signal is then simulated by using a preamplifier response function as measured on small scale double phase liquid argon TPC setups. Noise of a given amplitude can be added on top of the signal waveforms. Besides the generation of white noise, it is also possible to use a specific frequency spectrum that has e.g. been extracted from real data. The final step is the digitization of the generated waveforms.

Chapter 2

Reconstruction

The raw data from the near and far detectors provide highly detailed views of neutrino interactions and background events, which must be reduced and interpreted in order to extract the physics measurements. Cosmic rays must be identified and rejected, tracks and showers selected, particle identities assigned to the reconstructed objects, and event-level interpretations formed. While the performance of the reconstruction in both the Near Detector and the Far Detector have direct impacts on the physics sensitivity of the experiment, effects resulting from the detector designs and the angular and momentum acceptance differences of the near and far detectors are ingredients in the systematic uncertainty estimations that also affect the sensitivity of the experiment. If a particular class of events has a different reconstruction efficiency or energy resolution in the near and the far detectors, then modeling of the fraction of events in this class may become important, and cross sections and nuclear modeling systematic uncertainties can enter in this way. The fact that the near detector is smaller than the far detector and accepts a larger angular range of particles from the beam will introduce some of the systematic uncertainties even if the technologies are the same.

2.1 Near Detector Reconstruction

The Near Detector full reconstruction has not been developed yet, though a parameterized event reconstruction of the ND FastMC (described in section 1.1) has been developed and used for physics sensitivity studies. In the ND FastMC, particles are “reconstructed” by applying the smearing function shown in Tab. ???. The parameters of the smearing function are guided by NOMAD detector performance [?]. Fig. ?? shows the momentum resolution in ν_μ -CC obtained from the ND FastMC simulation and reconstruction framework with DUNE ND flux.

Along with the GEANT4 full simulation of the near detector, additional effort will be directed towards reconstruction with the aim of guiding the optimization of the near detector design by 2018.

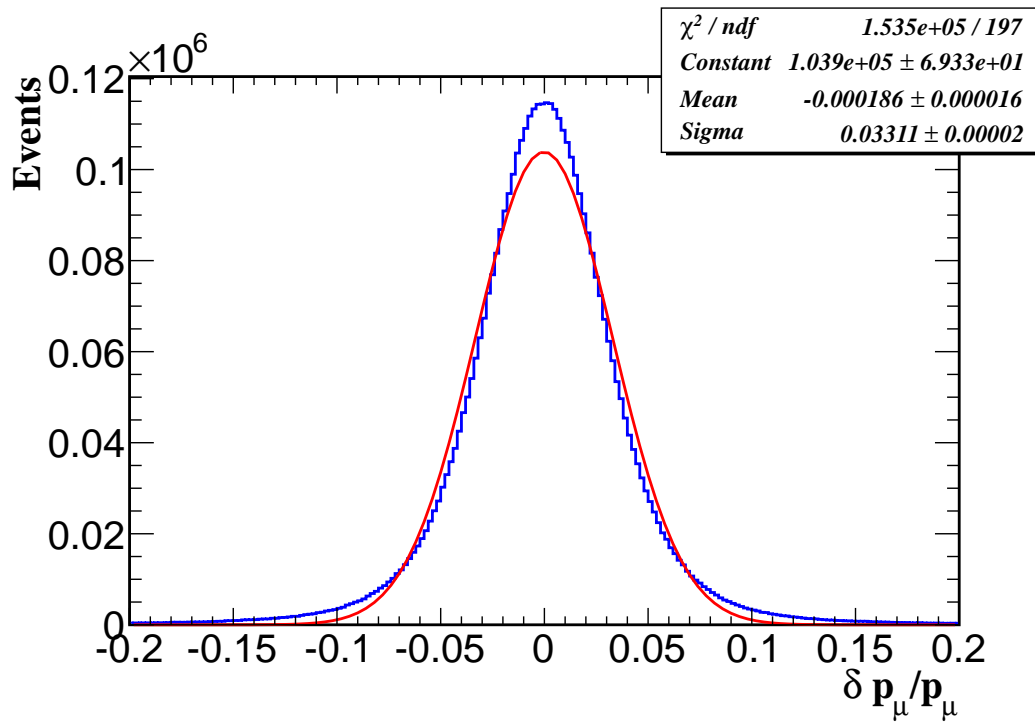


Figure 2.1: The distribution of fractional differences of measured muon momenta from their true values for smeared muon tracks in ν_μ -CC events using the Near Detector's FastMC parameterization. The distribution of $\delta p_\mu / p_\mu$ is shown with a blue histogram and a fit to a single Gaussian is shown with a red curve. The Gaussian fit gives an average resolution of 3.3%.

fig:ndfa

2.2 Far Detector Reconstruction

The reconstruction of particle interactions in Liquid Argon TPC detectors is an active area of research and development. A series of sophisticated reconstruction algorithms are required to address a broad range of complex event topologies, and to perform precise physics measurements that fully exploit the spatial and calorimetric precision offered by Liquid Argon technology. Although the field is not yet mature, there has been considerable progress in recent years, including the first fully automated pattern recognition algorithms.

A fully automated event reconstruction is being developed for the DUNE Far Detector, and major pieces are in place and functioning. The single-phase reconstruction algorithms are developed in LArSoft [?], which is based on the *art* framework [?]. The dual-phase reconstruction algorithms are incorporated in Qscan [?]. The block diagram in Figure 2.1 illustrates the components of the far detector reconstruction chain. The main steps and their ordering is similar between the single-phase and the dual-phase software designs and may evolve as experience is gained. The first stage involves the processing of the noisy ADC wire signals, and creation of 2D ‘hits’. A series of pattern recognition algorithms are then used to group the hits into 2D and 3D clusters representing individual particle tracks and showers. A set of high-level tools then reconstructs the vertex and 3D trajectory of each particle, provides particle identification, and reconstructs the four-momentum. While each step of the reconstruction chain has been implemented, the algorithms have not yet been fully optimized. The following sections describe the current status of each task.

2.2.1 Signal Processing and Filtering

A series of signal processing algorithms has been developed to perform noise reduction and baseline subtraction on the digital waveforms read out by Liquid Argon TPC detectors.

The TPC data are first uncompressed and put into local storage, one channel at a time. In the case that the DAQ writes data records to persistent storage the correspond to inconveniently long time periods, the data may be split into smaller events at the readin stage. At this stage, if an interaction is found to have taken place near the edge of the time corresponding to one record from the DAQ, the next DAQ record may be appended to make an offline event that corresponds to what is required to analyze the interaction of interest.

Single-Phase Signal Processing and Filtering

The single-phase detector’s bipolar induction-plane pulses must be deconvolved, since the negative portions of pulses may cancel positive portions of pulses on the channel that are nearby in time, even if the charge in those pulses is deposited on distant segments of the wire. Deconvoluting the bipolar signals produces unipolar pulses that can be fit in the same way as for the collection plane’s unipolar signals. The electronics response as well as the detector response is included in the deconvolution, and so deconvolution also of the collection-plane signals is also performed to

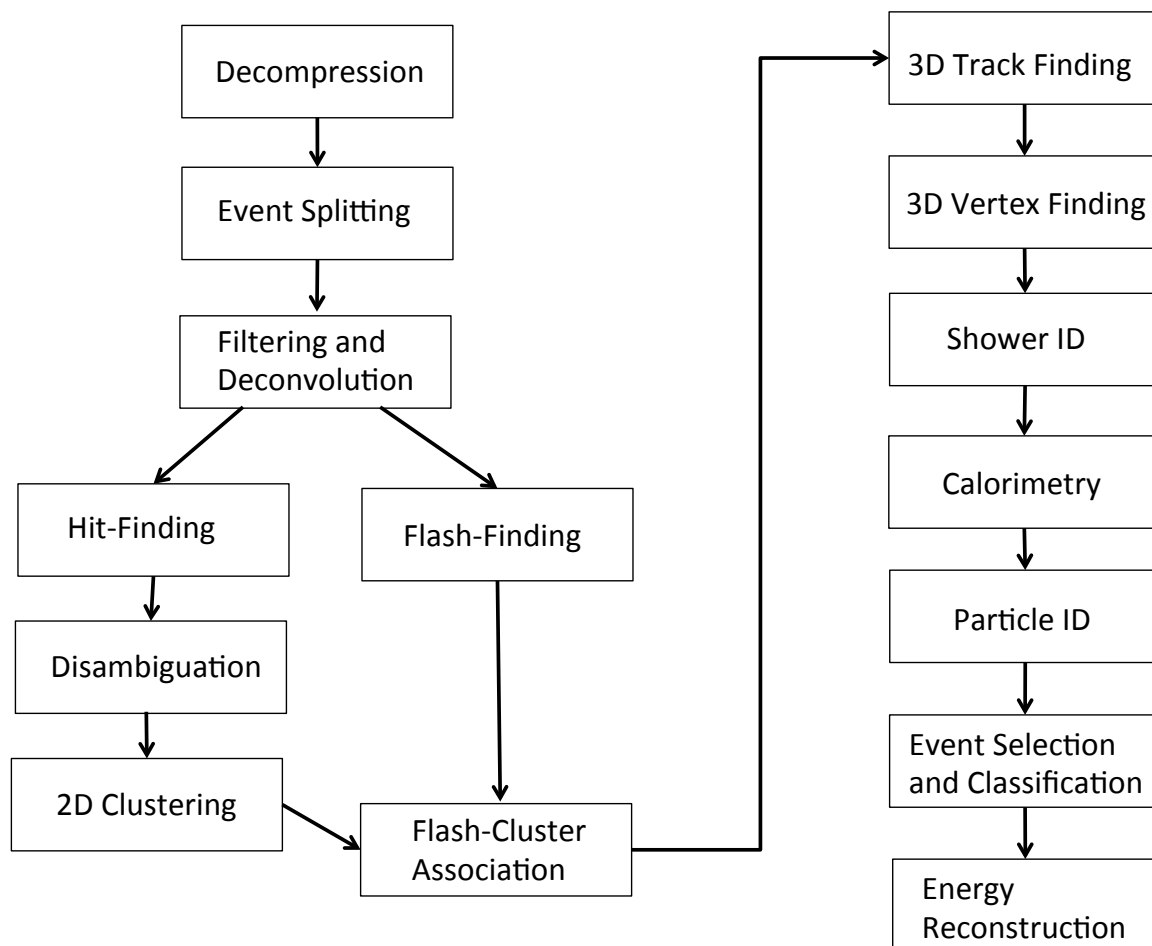


Figure 2.2: Block diagram showing the components of the far detector reconstruction chain

fig:fdre

improve the resolution. Since the deconvolution is performed by multiplying the Fourier transform of the input raw data by a deconvolution kernel, it is convenient to apply a frequency-dependent noise filter at this stage before transforming the data back into the time domain. A computational speedup is achieved by packing data in blocks that exceed thresholds plus nearby neighbors in time so that the FFT only needs to see a fraction of the total ADC samples collected in each event. The detector response functions used to construct the deconvolution kernels are currently based on *a priori* predictions, but these will be tuned and validated using data from the 35-ton prototype and the *Full-Scale Detector Engineering Test and Test Beam Calibration of a Single-Phase LArTPC* at CERN. It may be necessary to filter unipolar signal components on the induction-plane wires and handle these signals separately, in the case of partial non-transparency of the induction planes, which might be unavoidable near the wrapping boundaries.

Dual-Phase Signal Processing and Filtering

Qscan [?] also provides a set of methods for signal processing. The raw waveforms are first processed: this involves noise reduction as well as the subtraction of the baseline. Hits, defined as signals that are discriminated from the noise, are identified and reconstructed. In order to suppress noise without affecting the signal component too much, hence improving the signal to noise ratio, two different algorithms are used: the Fast Fourier Transform (FFT) filter, and the coherent noise subtraction algorithm. A smooth cut-off, implemented with a Fermi potential, efficiently suppresses the noise without introducing artifacts in the time domain. The coherent noise filter is implemented to remove identical noise patterns that are seen on larger sets of readout channels. Unlike in the case of the FFT filter, which directly suppresses the frequencies of single channels and thus reducing the signal bandwidth, the coherent noise filter ideally subtracts only the noise while keeping the signals unchanged. After suppressing the noise, the (constant) pedestal of each waveform has to be computed and subtracted from each sample.

2.2.2 TPC Hit Finding

Once deconvolved, raw ADC values trace out pulses, which are the best estimates of when charge arrived on a particular electronics channel. The widths of these pulses are determined by the detector resolution, by diffusion, and by the intrinsic width of the charge formation volume projected along the electric field direction, which can be quite long in the case of showers or tracks nearly aligned with the electric field. Multiple particles may contribute charge to the same pulse, which is expected to be the case frequently in dense electromagnetic showers, but can also occur from different particles leaving charge on segments of the wire that are far apart, as the data from a wire do not tell where along the wire the charge was deposited. Due to the wrapping of the induction-plane wires, pulses can contain charge from opposite sides of the APA, but not for collection-plane signals.

33 Single-Phase Hit Finding

1 Hits are reconstructed pulses on each TPC DAQ channel. Regions of interest are identified in the
 2 stream of deconvolved ADC samples, and sums of Gaussian functions are fitted to the data using
 3 MINUIT [19]. The peak position, the width, the area, and the sum of the deconvolved ADC values
 4 corresponding to the fitted Gaussian are recorded. In the case that multiple overlapping Gaussian
 5 fits are the best model of the data, the ADC sums are calculated for the entire region of interest,
 6 and then divided among the contributing hits proportional to their fit areas.

7 Dual-Phase Hit Finding

8 In Qscan, hits have to be extracted from the signal waveforms by means of a standard threshold
 9 discrimination. Due to changing noise conditions, the threshold is defined in relation to the mea-
 10 sured RMS noise value, which is measured for each event and readout strip, using the pre-trigger
 11 samples. In the general case there can be several close or overlapping tracks per event, producing
 12 a superposition of several signals/hits on a single readout strip. The shaping time constants of the
 13 preamplifiers are chosen such that double tracks being separated by a few μs can be resolved. The
 14 hit finding algorithms therefore extract multiple hit information by fitting the waveform function of
 15 the signal. The main parameters determined for the fitted hits are the hit time and the hit integral:
 16 together with the location of the corresponding readout channel, the hit time directly provides the
 17 information of the hit location in the considered view (projection), whereas the hit integral is
 18 related to the produced ionization charge and therefore provides the calorimetric information.

19 Single-Phase Disambiguation

20 A feature of liquid argon TPC geometries is that the location along a wire at which charge is
 21 deposited is not measured, creating a one-dimensional continuous ambiguity in the interpretation
 22 of the hits on a wire. As such, the planes of the TPC read out two-dimensional “views” of the
 23 three-dimensional events. The wrapping of the induction-plane wires in the DUNE APA design
 24 introduces another discrete ambiguity – the several wire segments that are connected together
 25 to form a DAQ channel all contribute charge on that DAQ channel, and it is not known from
 26 the wire’s signal which of those segments generated the charge. This discrete ambiguity must
 27 be broken before downstream reconstruction programs can do their work. The disambiguation
 28 procedure constitutes the first pattern recognition stage in the single-phase detector.

29 The detector geometry is chosen so that no induction-plane wire crosses any collection-plane wire
 30 more than once, necessitating a shallower induction-plane wire angle of 35.7° . The design from
 31 the LBNE CDR [20] proposed 44.3° and 45.7° as the angles of the U and V wire planes, which
 32 necessitated associating triplets of U , V , and Z hits in order to break the ambiguity. Hit triplets
 33 consistent in drift time and with only one possible combination of U , V , and Z hits that intersect
 34 in one position in space are determined to be “trivially” disambiguated. More complicated cases
 35 where multiple possible hits in other planes can be associated with a hit in a given plane, are dis-
 36 ambiguated by looking at nearby unambiguous hits and clustering them together. Misassociation

of hits in the three views, caused mainly by multiple charge deposits arriving at the same time, can cause choosing the incorrect wire segment.

The triplet-association algorithm is expected to work very well in the 35.7° geometry, by making few misassociations for the trivially disambiguated sample. Figure 2.2 shows the disambiguation performance for 6 GeV electrons and muons in the 35.7° far detector geometry. The algorithm used was developed for 35-ton event reconstruction, and has not yet been optimized for the 35.7° far detector geometry. Nonetheless, the performance is quite good, with a negligible fraction of mis-disambiguated hits, while the fraction of un-disambiguated hits can be lowered by improving the clustering step. A change request was granted in 2014 to move from the 44.3° , 45.7° wire angles to the shallower angle of 35.7° in order to improve the expected disambiguation performance.

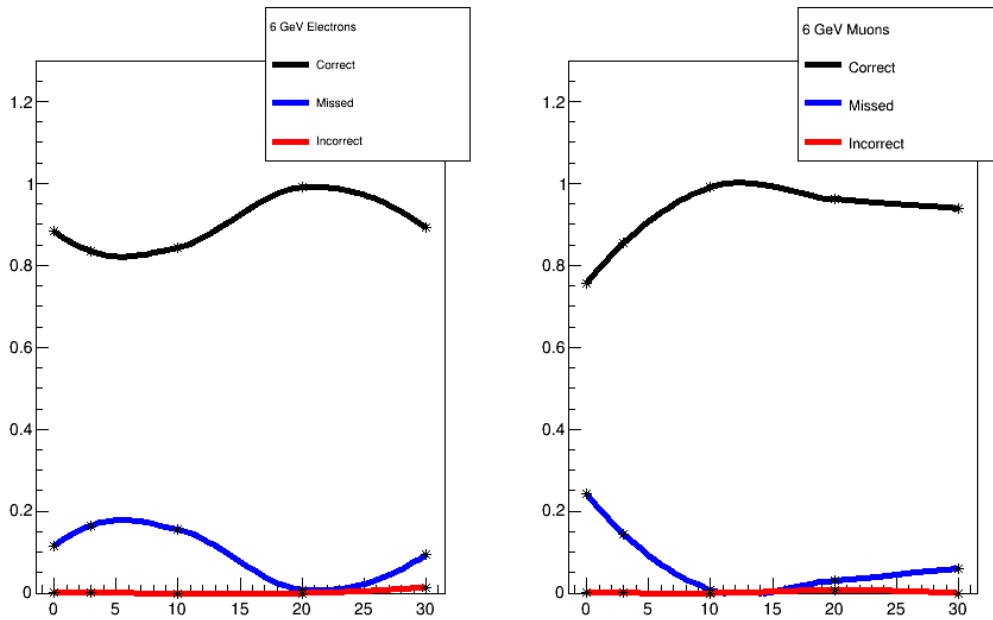


Figure 2.3: Simulated performance of the 35-ton disambiguation algorithm applied to the single-phase Far Detector design, for 6 GeV electrons and muons, shown separately as functions of the angle of the initial particle with respect to the plane parallel to the anode wires. The black curve shows the fraction of hits that are correctly disambiguated, the red curve shows the fraction of hits that are assigned the wrong wire segment, and the blue curve shows the fraction of hits that remain ambiguous, to be addressed by optimizing the algorithm.

2.2.3 Photon Detector Signal Reconstruction

The photon detector signals are reconstructed in two steps. First, a hit finder identifies signals on an individual channel, looking for peaks while account for noise and pedestal. Each hit is assigned a total integrated charge and a time associated with the first peak, since the SiPM signals are asymmetric and multiple individual photons may get grouped together into a single hit if they are close in time. Second, a flash finder groups together hits from across multiple photon detectors which are coincident in time (a “flash” being a source of light in the detector like the scintillation

from the passage of a charged particle). Each flash has a total integrated charge determined from its constituent hits as well as a two-dimensional position determined by a charge-weighted average of the positions of the photon detectors. Since the photon detectors all sit in a single plane, only two dimensional position reconstruction is possible. Once a flash is reconstructed, it becomes a candidate t_0 for objects reconstructed by the TPC. If only a single track or shower is present in the detector near the time of the flash, the association is clear, but if there are multiple overlapping tracks a likelihood-based method associates a TPC object with its best matching flash.

2.2.4 TPC Hit Clustering

After the hit-finding and disambiguation stages have completed, a series of pattern recognition algorithms are applied to the 2D hits in order to identify the tracks and showers produced by individual final-state particles in an event. In Liquid Argon TPC detectors, the pattern recognition stage must perform two functions in order to reconstruct 3D particles from 2D hits: (a) identify the patterns of hits within each two-dimensional view that correspond to individual particles; (b) match up hits and trajectories between views in order to reconstruct particles as three-dimensional objects. The development of automated pattern recognition algorithms for Liquid Argon TPC detectors is a relatively new field, but several 2D and 3D algorithms have been implemented, using a range of different techniques. For example, the “Fuzzy Cluster” package is a suite of algorithms that performs two-dimensional clustering of hits using several techniques developed outside of HEP [21] [22] [23].

A promising suite of pattern recognition algorithms, that provides fully automated reconstruction of 3D particle tracks and showers from 2D hits, is the PANDORA software development kit [24, 25]. PANDORA implements a highly modular approach to pattern recognition, in which the final-state particles within an event are reconstructed using a large chain of focused algorithms, each designed to identify and handle a specific event topology. The reconstruction chain begins with a series of 2D pattern recognition algorithms that group together hits into clusters based on their topology and spatial proximity. The next stage of the chain is 3D track reconstruction, which uses a rank-three tensor to match up all possible combinations of 2D clusters between the U , V , and Z views, and group together the best-matched triplets or doublets of clusters. If necessary, 2D clusters are modified to improve the consistency of the 3D event. Once the 3D track trajectories have been identified, a series of vertex-finding algorithms are applied to the event, which reconstruct the neutrino interaction vertex by analyzing the 2D and 3D event topology. The remaining 2D clusters are then used to reconstruct electromagnetic and hadronic showers, first as extended 2D clusters, and then as 3D particles, using a similar procedure to 3D track reconstruction. Finally, a neutrino event is formed by connecting together the reconstructed tracks and showers at the interaction vertex.

The PANDORA pattern recognition algorithms have been developed using simulated neutrino interactions in the energy range 100 MeV – 25 GeV. Figure 2.3 shows some example events. Figure 2.4 shows the efficiency for reconstructing the leading final-state lepton in 5 GeV ν_e CC and ν_μ CC interactions, plotted as a function of momentum using the MicroBooNE detector geometry. In both samples, the reconstruction efficiency increases rapidly with momentum, rising above 90% at 500 MeV and reaching approximately 100% at 2 GeV. Figure 2.6 shows the spatial resolution for

reconstructing the primary interaction vertex in 5 GeV ν_μ CC events, projected onto the x , y and z axes. An estimate of the overall vertex resolution is obtained by taking the 68% quantile of 3D vertex residuals, which yields 2.2 cm (2.5 cm) for ν_μ CC (ν_e CC) events.

Algorithms specific for reconstruction with two views, as is the case for the dual-phase detector design, have been extensively developed as well. A preliminary 2D clustering is carried on similarly to what described above. A first-pass hit clustering, using a nearest-neighbor algorithm and association algorithms is performed for each projection. Then the primary vertex is identified based on the presumed beam direction and cluster positions and directions. Redundant information from all readout views is used to constrain the vertex location. Primary final-state particles (seed-clusters) are finally identified, based on cluster length and proximity to vertex, and each of the remaining non-seed clusters is associated with existing seed-clusters so that all energy deposits from a single final-state particle are grouped together. At the end of this process, clusters not directly related to the vertex, as ascertained either by pointing or position, will be associated with clusters coming from the vertex which are in close proximity, as long as there is not another vertex-related cluster nearby.

The PANDORA reconstruction has been tested on charged current events generated by both ν_e and ν_μ considering the processes $\nu_\ell \rightarrow \ell + p$ and $\nu_\ell \rightarrow \ell + p + \pi^+$. The neutrino energy distribution is simulated by means of a detailed beam flux simulation. Particles produced in the neutrino interactions were then generated by taking GENIE output, selecting only events with matching final state topologies, and simulating these events using Qscan. The performance has been tested by using truth information to associate each final-state particle with up to one reconstructed cluster. The quality of the neutrino event reconstruction is evaluated by performing hit-by-hit comparisons of simulated and reconstructed particles and calculating the following Monte-Carlo-based performance metrics: “completeness,” which is defined as the fraction of hits generated by the true particle and contained in the reconstructed cluster, and “purity,” which is defined as the fraction of hits in the reconstructed cluster that were deposited by the true particle. The “true particle” is defined to be the one that contributes the most hits to the reconstructed cluster. Both the completeness and purity are found to be above 90% for particles with energies above 800 MeV. Figure 2.5 shows purity and completeness metrics.

2.2.5 Track Fitting

The track reconstruction algorithms in a liquid argon TPC is divided into trajectory reconstruction and track parameter estimation. Hits are the input data for track reconstruction. Each hit represents a one-dimensional measurement of a track (the drift time) on a measurement surface defined by the charge drift direction and the readout wire. Hits from multiple views may be combined into three-dimensional space points. Three dimensional track reconstruction can proceed from space points or directly from hits.

The Kalman filter algorithm [26] has been widely used in high energy physics for track reconstruction. The Kalman filter provides an elegant mathematical solution to the problem of finding an optimal track description from a collection of candidate measurements that are hits or space points, especially in cases where the number of measurements is much larger than the five pa-

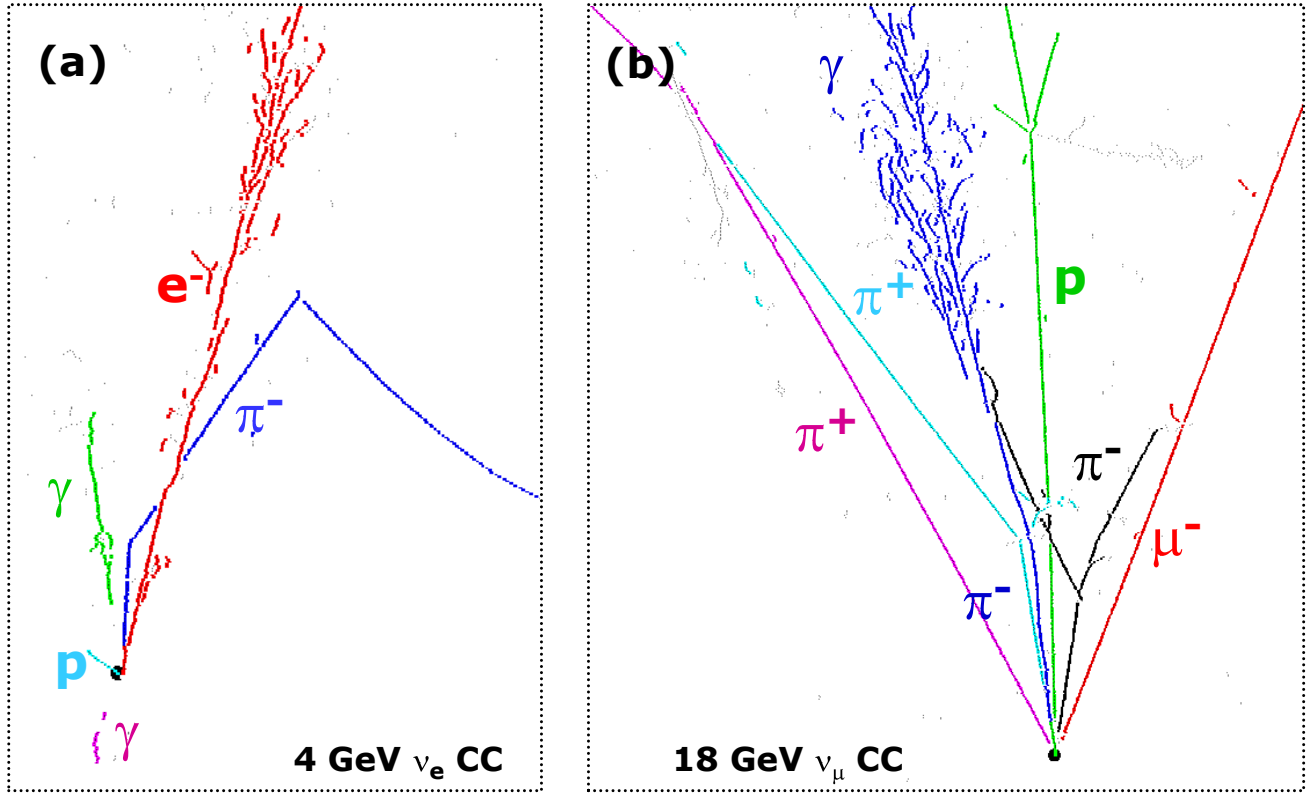


Figure 2.4: Two-dimensional event displays showing PANDORA clustering of the hits generated by a 4 GeV ν_e CC event (left) and a 18 GeV ν_μ CC event (right). The color-coding of the hits is from the automatic cluster algorithms but the particle ID labels have been added by hand.

fig:reco

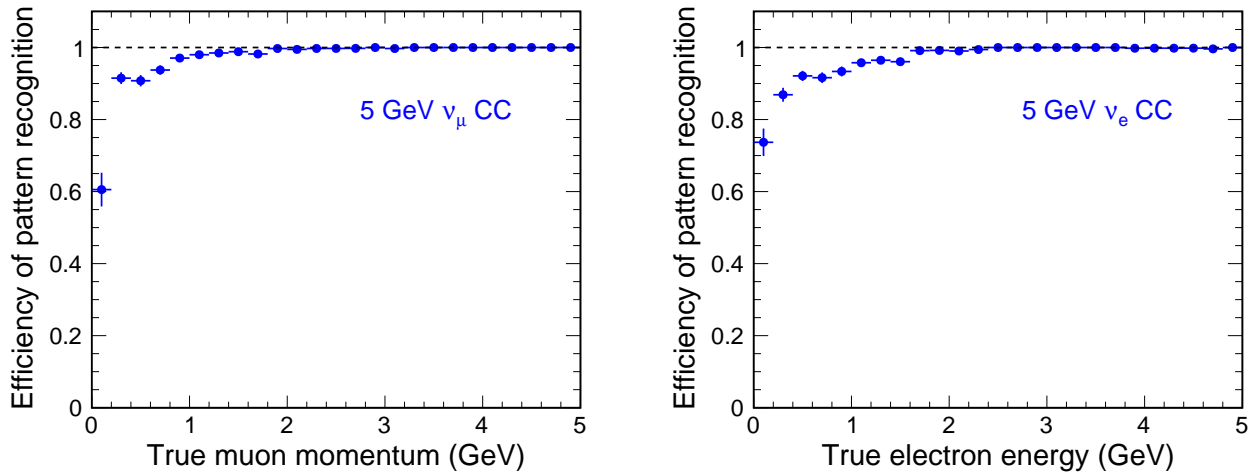


Figure 2.5: Reconstruction efficiency of Pandora pattern recognition algorithms for the leading final-state lepton in 5 GeV ν_μ CC (left) and ν_e CC (right) neutrino interactions, plotted as a function of the lepton momentum. The reconstruction performance is evaluated using the MicroBooNE detector geometry.

fig:reco

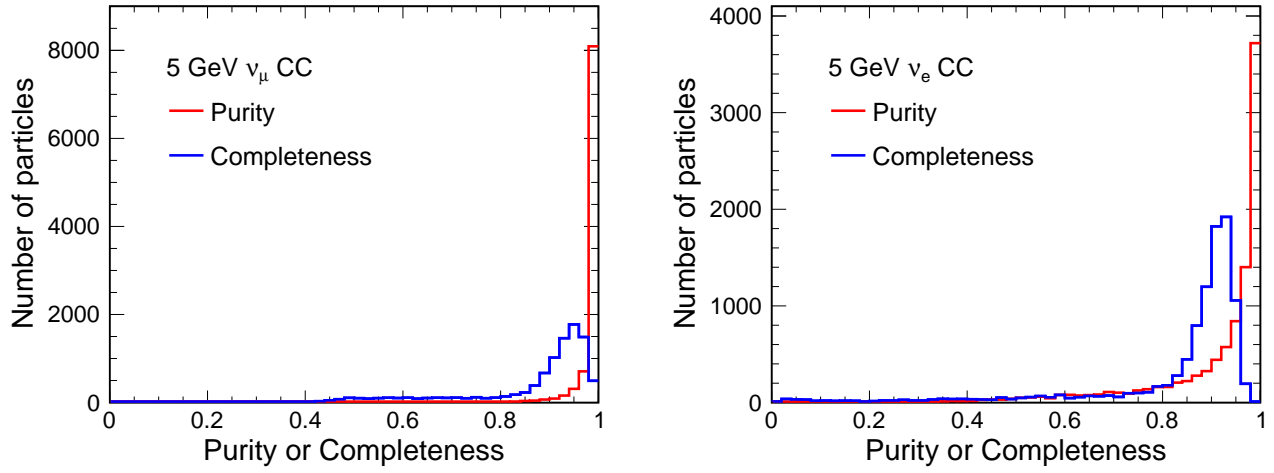


Figure 2.6: Distributions of purity and completeness for the PANDORA reconstruction of the cluster corresponding to the leading lepton for a large sample of 5 GeV ν_μ CC events (left) and a large sample of 5 GeV ν_e CC events (right).

fig:reco

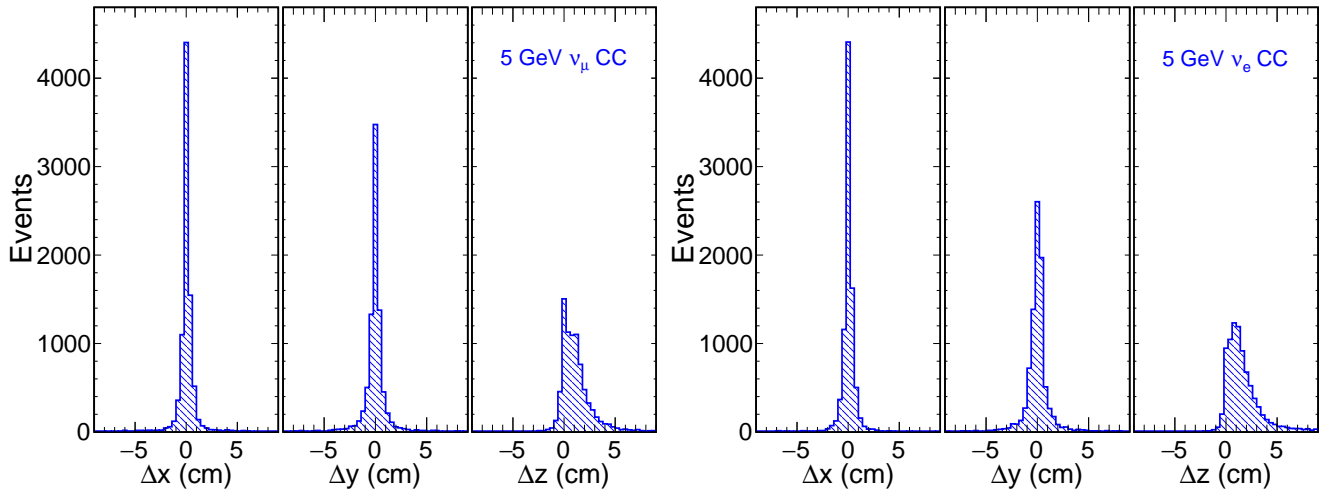


Figure 2.7: Distribution of 2D residuals between reconstructed and simulated interaction vertex for 5 GeV ν_μ CC (left) and ν_e CC (right) interactions in the MicroBooNE detector. The x axis is oriented along the drift field, the y axis runs parallel to the collection plane wires, and the z axis points along the beam direction.

fig:reco

rameters needed to specify a track on a surface. The Kalman filter can be used for both pattern recognition and parameter estimation. The Kalman filter technique has been applied to 3D track reconstruction by ICARUS [27], and is being studied by MicroBooNE. This technique incorporates the effects of multiple Coulomb scattering, enabling a scattering-based estimate of the track momentum, which is shown by ICARUS to be as good as $\Delta p/p \approx 10\%$, depending mainly on the track length [27]. The data from ICARUS have also been used to develop a precise track reconstruction, which builds a 3D trajectory for each track by simultaneously optimising its 2D projections to match the observed data [29]. Another promising technique, based on the local principal curve algorithm, has been implemented in conjunction with the development of the dual-phase detector concept, and is shown to provide a precise reconstruction of two-particle event topologies [30, 31], including precise vertex reconstruction. Figure 2.7 shows vertex resolution plots for the dual-phase detector design.

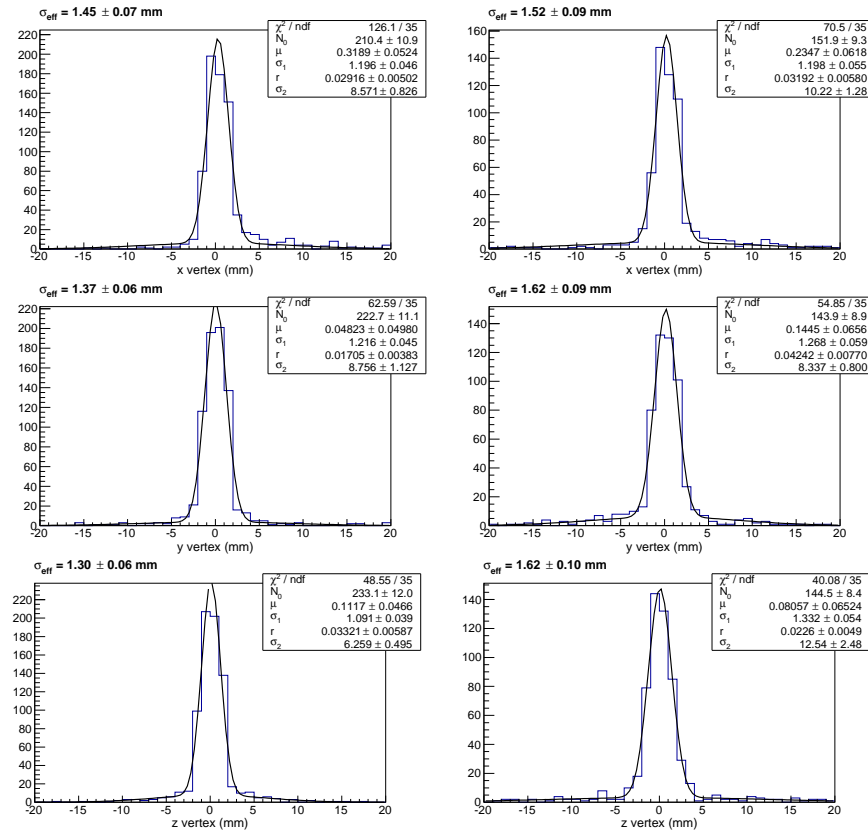


Figure 2.8: Spatial resolutions for the primary vertex reconstruction using local principal curves, separately in the x , y , and z directions, in a dual-phase detector. The left-hand column shows the resolutions for CCQE $\nu_\mu \rightarrow \mu + p$ events, and the right-hand column shows the resolutions for CCQE $\nu_e \rightarrow e + p$ events. The distributions are fit to a sum of two Gaussians with equal means. The effective width is quoted above each plot as $\sigma_{\text{eff}} = \sigma_1 + r \cdot \sigma_2$, where r is the ratio of amplitudes of the two Gaussian components.

2.2.6 Shower Measurement

The electromagnetic shower algorithms have two steps. The first is a post-clustering stage which examines the existing clusters in terms of their 2D parameters to determine whether the clusters

are shower-like or track-like. The selected shower-like clusters are examined to assign starting points, directions and angles in the wire-time plane. The second step is 3D shower reconstruction, which matches the 2D clusters between views in order to obtain 3D shower axes and start points. These 3D parameters allow the calculation of the shower energies and charge depositions at the starts of the showers, which are used in particle identification.

2.2.7 Calorimetry

As charged particles traverse a volume liquid argon, they deposit energy through ionization and scintillation. It is important to measure the energy depotion as it provides information on the particle energy and and helps to identify what type of particle it is. The algorithm for reconstructing the ionization energy in LArSoft is optimized for line-like tracks and is being extended to showers. For each hit on a reconstructed track, the hit area or amplitude, in ADC counts, is converted to the charge Q_{det} , in fC units, on the wire using an ADC to fC conversion factor. This factor is to be calibrated either *in situ* with muons or with test-stand measurements. To account for the charge loss along the drift due to impurities, a first correction is applied to Q_{det} to to account for the finite electron lifetime. We define Q_{free} as the free charge after recombination and before reattachment, and is given by $Q_{\text{free}} = Q_{\text{det}}/e^{-t/\tau_e}$, where t is the electron drift time for the hit and τ_e is the electron lifetime measured by the muons or purity monitors. The charge Q_{free} is divided by the track pitch dx , which is defined as the dot production of track direction and the direction normal to the wire direction in the wire plane, to get the dQ_{free}/dx for the hit. Finally, to account for charge loss due to recombination, also known as “charge quenching,” a second correction is applied to convert dQ_{free}/dx to dE/dx based on the modified box model [32] or Birks’s model[15]. The total energy deposition from the track is obtained by summing the dE/dx from each hit:

$$\sum_i^{\text{all hits}} (dE/dx)_i \cdot dx_i.$$

2.2.8 Particle Identification

If the incident particle stops in the LArTPC active volume, the energy loss, dE/dx , as a function of the residual range (R), the path length to the end point of the track, is used as a powerful method for particle identification. There are two methods in LArSoft to determine particle species using calorimetric information. The first method calculates four χ^2 values for each track by comparing measured dE/dx versus R points to the proton, charged kaon, charged pion and muon hypotheses and identifies the track as the particle that gives the smallest χ^2 value. The second method calculates the quantity PIDA = $\langle A_i \rangle = \langle (dE/dx)_i R_i^{0.42} \rangle$ [32], which is defined to be the average of $A_i = (dE/dx)_i R_i^{0.42}$ over all track points, indexed by i , where the residual range R_i is less than 30 cm. The particle species can be determined by making a selection on the PIDA value.

Another method was developed for the ICARUS reconstruction software and may be incorporated with LArSoft. The vector of probabilities p_i of each considered particle hypothesis (p , K^\pm , π^\pm , μ^\pm , or none of the above as the fifth hypothesis) is calculated for each measured point $q_j = (dQ/dx; R)$, where dQ is the calorimetric measurement (correction for the recombination effect is not required).

The probabilities p_i are obtained as outputs from a neural network trained on a set of $(dQ/dx; R)$ points calculated for reconstructed MC tracks. The final probabilities of each PID hypothesis are calculated as products of mutually independent p_i for all points along the tested track (similarly to the PIDA algorithm, the last 30 cm of the track is used). The same neural network outputs as functions of the dQ/dx and R variables are used to test the hypothesis if the incident particle is actually stopping.

The dE/dx information is also used for $e - \gamma$ discrimination, a method complementary to the topological discrimination. A cascade produced by an electron is expected to have a dE/dx characteristic of a single minimum-ionizing particle (MIP) in its initial part, before the shower develops. A cascade produced by a gamma converting to an e^+e^- pair is expected to have a two-MIP dE/dx in its initial part. An algorithm proposed for the reconstruction of the initial part of the cascade is based on Ref. [29]. A straight 3D segment with one endpoint fixed at the primary vertex position is created. The position of the other endpoint of the segment is optimized to minimize distances between the segment 2D projections and hits of clusters corresponding to the cascade initial part. The 3D length used to measure dE/dx is at most 2.5 cm. The method does not require explicit association of hits between 2D planes and is efficient also for a low number of hits. There are, however, event topologies in which the dE/dx reconstruction fails. The cascade initial part projection can be too short or it may be shadowed by the cascade itself if the cascade develops in a cone around an axis parallel to the readout wires. Such configurations may prevent the spatial reconstruction or may cause inaccurate dE/dx measurements if they occur for the collection plane, which is used for charge measurement. The efficiency of electron selection versus gamma rejection in the isotropic distribution of cascades is illustrated in Fig. 2.8 (simulation prepared with FLUKA [?, ?] for the single-phase configuration as foreseen for the far detector). The curves in the figure are obtained for varying the cut on the reconstructed dE/dx value. The effect of unfavorable spatial orientations of the cascade can be practically eliminated if the charge measurement can be performed also with the induction planes. Another source of inefficiency in this method occurs mainly in the low energy range, and is related to the contribution of cascades from gammas undergoing Compton scattering, which produces a single MIP dE/dx , or gammas that convert into e^+e^- pairs with a large asymmetry in their energies, which produces a flat distribution in dE/dx between single and double MIP rates. The dependence on the cascade energy of the performance of $e - \gamma$ separation using dE/dx is illustrated in Fig. 2.9.

2.2.9 Neutrino Event Reconstruction and Classification

In Qscan, a multivariate analysis (MVA) was used to separate particle types based on the spatial characteristics of their clusters [33, 31, ?]. First step performs a principal components analysis (PCA), transforming the axes to lie along the cluster direction and perpendicular to it. Several quantities are then calculated to characterize the cluster: the lateral spread, the mean charge-weighted inverse distance of hits to the primary cluster axis (this is expected to distinguish effectively between showers and tracks), the dE/dx . These variables are then fed into Boosted Decision Trees analyses, each calculating the signal and background likelihoods for a particular particle hypothesis. Currently muon, electron, proton and charged pion hypotheses are considered. It is anticipated that these likelihoods will be used in various ways by downstream analysis code, depending on the needs of the specific analysis. In the present analysis, the BDT results for muon

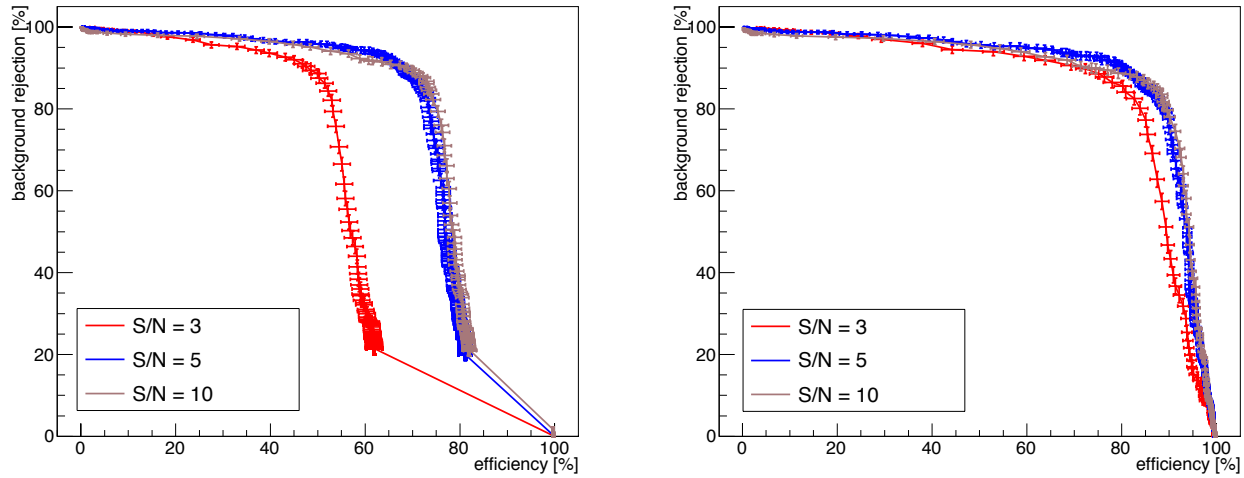


Figure 2.9: Performance of the $e - \gamma$ separation algorithm using the ionization density of the initial part of the EM shower, as functions of the assumed signal to noise ratio S/N . Left panel: photon rejection vs. electron efficiency for all events. Right panel: the same, but only for events with sufficient hits in the initial part of the shower to reconstruct it well (see text).

fig:egam

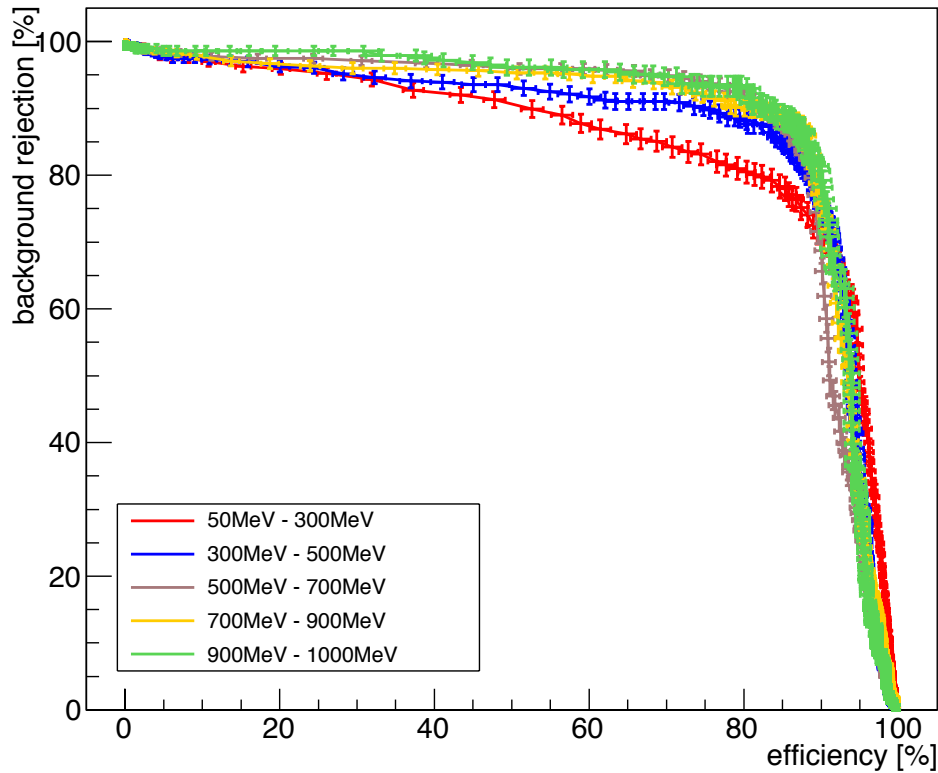


Figure 2.10: Performance of the $e - \gamma$ separation algorithm using the ionization density of the initial part of the EM shower, as functions of the energy of the electron or photon. Only events with well-reconstructed initial portions of the shower are included (see text).

fig:egam

and electron hypotheses are used to identify lepton clusters and classify events. The signal and background distributions for these hypotheses are shown in Figure 2.10.

The overall performance of the reconstruction chain (from clustering to PID) has been estimated with a simple binned lepton flavor analysis, to understand its ability to distinguish ν_e and ν_μ events. If a single lepton flavor is identified in the event, then the event is considered as a signal event of the observed lepton flavor. If neither or both lepton flavors are identified, the event is discarded. Numbers of events correctly reconstructed is above 90% for ν_μ -CCQE events.

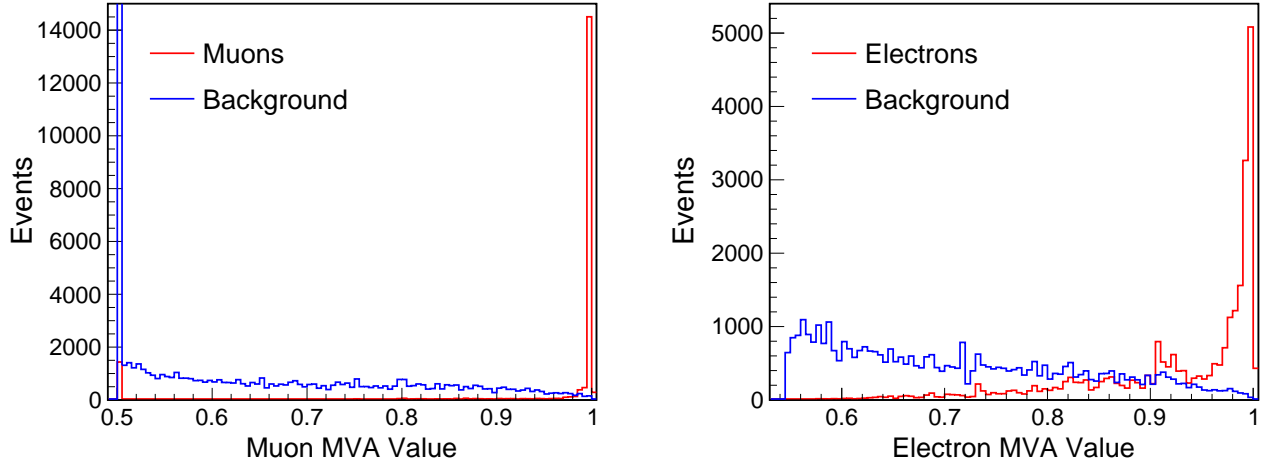


Figure 2.11: Plots showing signal and background distributions for electron (a) and muon (b) MVA hypotheses. Background consists of all particles not corresponding to the relevant signal type.

For accepted events, the neutrino energy is estimated assuming a CCQE event and using the two-body approximation, and also calorimetrically. The calorimetric reconstruction takes account of the quenching factors for the different particles by assuming that all hits not associated with the lepton cluster are due to hadronic activity. Figure 2.11 shows the results of the kinematic energy reconstruction for CCQE events, and Figure 2.12 the results of the calorimetric energy reconstruction. It is seen that for high-energy muons, the measured energy saturates. This is due to the muon escaping the detector volume.

2.2.10 Calibration

In order to meet the requirements of high detection efficiency, efficient and pure particle identification, excellent energy resolution, and small systematic uncertainties on these performance parameters, calibrations of the detector will be needed. *In situ* calibration techniques using data collected by the FD under identical conditions as used for physics analyses are the most desirable. These include studying cosmic-ray events and non-fiducial interactions. But not all performance measures can be calibrated in this way. A laser calibration system will constrain the detector alignment as well as measure any residual space-charge effects (which are expected to be very small underground) and other sources of field non-uniformity, as well as provide timing calibration

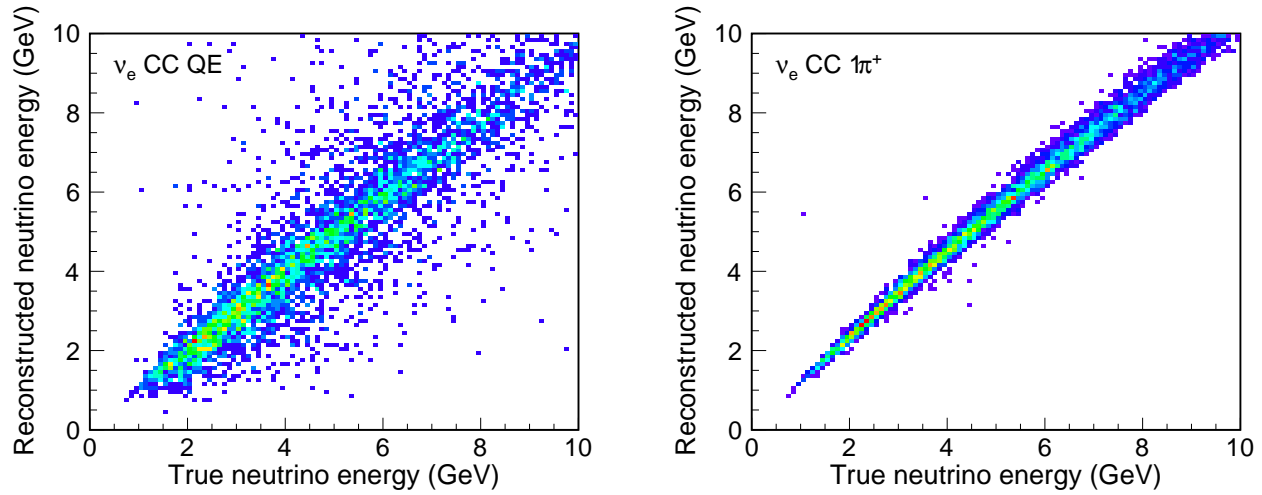


Figure 2.12: Dual-phase LArTPC neutrino energy measurement. Distributions of reconstructed neutrino energy versus true neutrino energy, assuming two-body kinematics. Plots shown are for ν_e CCQE (a) and ν_μ CCQE (b).

fig:reco

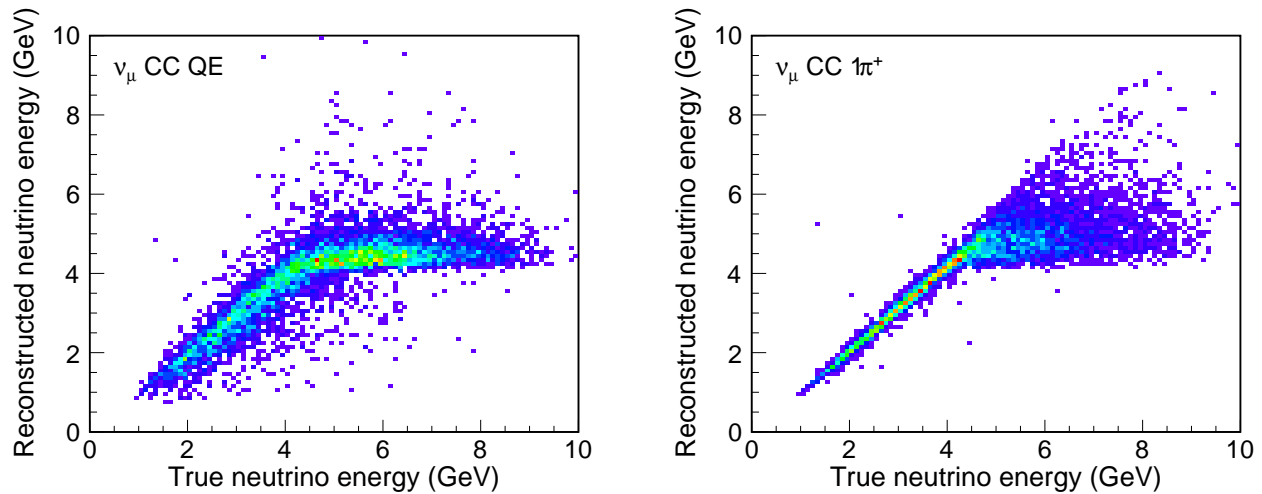


Figure 2.13: Dual-phase LArTPC neutrino energy measurement. Distributions of reconstructed neutrino energy versus true neutrino energy, using calorimetric energy estimation. Plots shown are for ν_e CC $1\pi^+$ (a) and ν_μ CC $1\pi^+$ (b).

fig:reco

14 and crosscheck the response to drifting charge. The electronics will be outfitted with charge-
15 injection calibration systems so that non-uniformities in the electronics response can be corrected
16 in a time-dependent fashion. The response to charged particles of known energy and particle type
17 will rely on test-beam data from LArIAT and the CERN test experiments *Full-Scale Detector En-*
18 *gineering Test and Test Beam Calibration of a Single-Phase LArTPC* and *Long Baseline Neutrino*
19 *Observatory Demonstration (WA105)*.

References

- [1] S. Agostinelli *et al.*, “GEANT4 — A Simulation Toolkit,” *Nucl. Instrum. Methods*, vol. A, no. 506, pp. 250–303, 2003.
- [2] J. Allison *et al.*, “GEANT4 developments and applications,” *IEEE Trans. Nucl. Sci.*, vol. 53, no. 1, pp. 270–278, 2006.
- [3] P. Adamson *et al.*, “LArIAT: Liquid Argon TPC in a Test Beam.” FERMILAB-PROPOSAL-1034, 2013.
- [4] <http://t962.fnal.gov/>.
- [5] R. Acciarri *et al.*, “A study of electron recombination using highly ionizing particles in the ArgoNeuT Liquid Argon TPC,” *JINST*, vol. 8, p. P08005, 2013.
- [6] F. Cavanna, M. Kordosky, J. Raaf, and B. Rebel, “LArIAT: Liquid Argon In A Testbeam.” arXiv:1406.5560, 2014.
- [7] H. Chen *et al.*, “Proposal for a New Experiment Using the Booster and NuMI Neutrino Beamlines: MicroBooNE.” FERMILAB-PROPOSAL-0974, 2007.
- [8] B. J. P. Jones, “The Status of the MicroBooNE Experiment,” *PoS*, vol. EPS-HEP2011, p. 436, 2011.
- [9] MicroBooNE Collaboration, “The MicroBooNE Conceptual Design Report.” <http://microboone-docdb.fnal.gov/cgi-bin/ShowDocument?docid=1821>, 2010.
- [10] C. Andreopoulos *et al.*, “The GENIE Neutrino Monte Carlo Generator,” *Nucl. Instrum. Methods*, vol. A, no. 614, pp. 87–104, 2010.
- [11] C. Hagmann, D. Lange, J. Verbeke, and D. Wright, “Cosmic-ray Shower Library (CRY),” tech. rep., Lawrence Livermore National Laboratory, 2012. UCRL-TM-229453.
- [12] C. Hagmann, D. Lange, J. Verbeke, and D. Wright, “Monte Carlo Simulation of Proton-induced Cosmic-ray Cascades in the Atmosphere,” tech. rep., Lawrence Livermore National Laboratory, 2012. UCRL-TM-229452.

- [13] C. Hagmann, D. Lange, J. Verbeke, and D. Wright. <http://nuclear.llnl.gov/simulation/main.html>.
- [14] R. Chytrcek, J. McCormick, W. Pokorski, and G. Santin, “Geometry Description Markup Language for Physics Simulation and Analysis Applications,” *IEEE Trans. Nucl. Sci.*, vol. 53, pp. 2892–2896, 2006.
- [15] J. B. Birks, *The Theory and practice of scintillation counting*. Pergamon Press, 1964.
- [16] T. Doke, H. Crawford, A. Hitachi, J. Kikuchi, P. Lindstrom, *et al.*, “Let Dependence of Scintillation Yields in Liquid Argon,” *Nucl.Instrum.Meth.*, vol. A269, pp. 291–296, 1988.
- [17] M. Szydagis, A. Fyhrie, D. Thorngren, and M. Tripathi, “Enhancement of NEST Capabilities for Simulating Low-Energy Recoils in Liquid Xenon,” *JINST*, vol. 8, p. C10003, 2013.
- [18] M. Szydagis, N. Barry, K. Kazkaz, J. Mock, D. Stolp, *et al.*, “NEST: A Comprehensive Model for Scintillation Yield in Liquid Xenon,” *JINST*, vol. 6, p. P10002, 2011.
- [19] F. James, “MINUIT Function Minimization and Error Analysis: Reference Manual Version 94.1.” CERN-D-506, CERN-D506, 1994.
- [20] LBNE Collaboration, “The LBNE Conceptual Design Report.” LBNE DocDB 5235, 4317, 4724, 4892, 4623, 5017, 2012.
- [21] L. Fu and E. Medico, “FLAME, a novel fuzzy clustering method for the analysis of DNA microarray data,” *BMC Bioinformatics*, vol. 8, p. 3, 2007.
- [22] J. Matas *et al.*, “Robust Detection of Lines Using the Progressive Probabilistic Hough Transform,” *Computer Vision and Image Understanding*, vol. 78, pp. 119–137, 2000.
- [23] M. Ester, H. Peter Kriegel, J. S, and X. Xu, “A density-based algorithm for discovering clusters in large spatial databases with noise,” in *Proceedings of the Second International Conference on Knowledge Discovery and Data Mining (KDD-96)*, pp. 226–231, AAAI Press, 1996.
- [24] J. Marshall and M. Thomson, “Pandora Particle Flow Algorithm,” in *Proceedings, International Conference on Calorimetry for the High Energy Frontier (CHEF 2013)*, pp. 305–315, 2013.
- [25] J. Marshall and M. Thomson, “The Pandora software development kit for particle flow calorimetry,” *J.Phys.Conf.Ser.*, vol. 396, p. 022034, 2012.
- [26] R. Kalman, “A New Approach to Linear Filtering and Prediction Problems,” *J. Fluids Eng.*, vol. 82, pp. 35–45, 1960.
- [27] A. Ankowski *et al.*, “Measurement of through-going particle momentum by means of multiple scattering with the ICARUS T600 TPC,” *Eur.Phys.J.*, vol. C48, pp. 667–676, 2006.

- 21 [28] “FIXME,” FIXME. FIXME.
- 22 [29] M. Antonello, B. Baibussinov, P. Benetti, E. Calligarich, N. Canci, *et al.*, “Precise 3D track re-
23 construction algorithm for the ICARUS T600 liquid argon time projection chamber detector,”
24 *Adv.High Energy Phys.*, vol. 2013, p. 260820, 2013.
- 25 [30] J. Back, G. Barker, S. Boyd, J. Einbeck, M. Haigh, *et al.*, “Implementation of a local prin-
26 cipal curves algorithm for neutrino interaction reconstruction in a liquid argon volume,”
27 *Eur.Phys.J.*, vol. C74, p. 2832, 2014.
- 28 [31] “Final report of the LAGUNA-LBNO design of a pan-European infrastructure for large ap-
29 paratus studying Grand Unification, Neutrino Astrophysics and Long Baseline Neutrino Os-
635 cillations (Funded by European Commission FP7 Research Infrastructures, grant agreement
636 number: 284518),” *Annex*.
- 637 [32] J. Thomas and D. Imel, “Recombination of electron-ion pairs in liquid argon and liquid xenon,”
638 *Phys.Rev.*, vol. A36, pp. 614–616, 1987.
- 639 [33] L. A. et al., “LBNO-DEMO: Large-scale neutrino detector demonstrators for phased per-
640 formance assessment in view of a long-baseline oscillation experiment, The LBNO-DEMO -
641 WA105 - Collaboration,” *CERN-SPSC-2014-013; SPSC-TDR-004*, 2014.
- 642 [34] “FIXME,” FIXME. FIXME.